

Fiber buckling in confined viscous flows: an absolute instability described by the Ginzburg-Landau equation

Jean Cappello¹, Olivia du Roure¹, François Gallaire², Camille Duprat³, and Anke Lindner¹

¹ *PMMH, ESPCI, Paris, France*

² *LMFI, EPFL, Lausanne, Switzerland*

³ *LadHyX, École Polytechnique, Palaiseau, France*

(Dated: January 23, 2022)

We explore the dynamics of a flexible fiber transported by a viscous flow in a Hele-Shaw cell of height comparable to the fiber height. We show that long fibers aligned with the flow experience a buckling instability. Competition between viscous and elastic forces leads to the deformation of the fiber into a wavy shape convolved by a Bell-shaped envelope. We characterize the wavelength and phase velocity of the deformation as well as the growth and spreading of the envelope. Our study of the spatio-temporal evolution of the deformation reveals a linear and absolute instability arising from a local mechanism well described by the Ginzburg-Landau equation.

The dynamics of a flexible fiber transported in a flow results from a coupling between deformation and transport and exhibits rich behaviours [1] including bending [2–4], buckling [4–7] or coiling [8]. Such dynamics have been studied in different types of flows including simple shear flows [9–13], vortex arrays [6, 7, 14, 15], Poiseuille flows [16], extensional flows [5, 8, 17, 18] or sedimentation in quiescent fluids [3, 4, 19]. The transport dynamics of flexible fibers in confined geometries has only recently been explored [2, 20, 21], and shows even richer dynamics, as a consequence of the interaction between the fiber of evolving shape, and the confining walls.

In this study, we focus on the dynamics of a flexible fiber transported by a pressure-driven flow in a Hele-Shaw cell (see Fig. 1). The fiber is aligned with the flow

and is confined by the channel top and bottom walls. Typical experimental observations can be seen in Fig. 1 (a) showing the shape of a flexible fiber during transport along the microchannel. The fiber, initially straight, deforms into a sinusoidal shape with a very well defined wavelength modulated by a bell-shaped envelope. The dynamics of the deformation is manifold: the amplitude of the deformation increases with time, the perturbation travels along the fiber from back to front and the envelope broadens along the fiber while remaining centered at a fixed lengthwise position.

Such dynamical shape changes can be triggered through various mechanisms amplifying initial perturbations, classified as either global or local instabilities. Global instabilities span the entire domain (here the fiber) and couple the two end conditions. Hence the boundary conditions are essential in the selection of the deformation mode. This is typically the case for classical buckling instabilities where the perturbation ranges over the entire fibre and the perturbation wavelength is function of the fiber length [1].

On the contrary, in the presence of a local amplifying mechanism the deformations result from an initial disturbance invading the unstable system via propagating fronts. If the perturbation grows but is simultaneously advected such that the disturbance eventually decays at any fixed point, it ultimately leaves the fiber and the instability is said to be convective. In contrast, as is the case here, if the perturbation grows at a fixed spatial position, it eventually invades the entire fiber leading to a self-sustained instability and is said to be absolute.

Absolute instabilities have been observed in open flow hydrodynamics, such as the flow past bluff bodies (Bénard-von Kármán vortex street) [22], parallel shear flows [23–25], transition from dripping to jetting [26–29] or the flow of viscous films down vertical fibers [30, 31]. However, absolute instabilities resulting in the deformation of a flexible object in interaction with viscous flows have not been reported yet. In this letter we describe a one-dimensional example of such an instability develop-

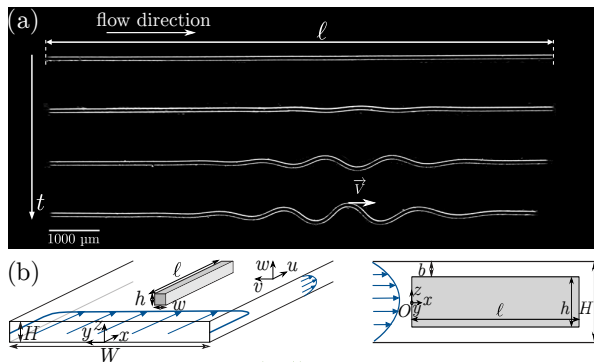


FIG. 1: (a) Chronophotographies of a parallel fiber transported by the external flow in the moving reference frame of the fiber. Time increases from top to bottom (time interval is 4 sec). The phase velocity is denoted \vec{V} and the horizontal arrow illustrates the direction of the perturbation propagation. The flow velocity, from left to right, is $u_0 = 0.65 \text{ mm}\cdot\text{s}^{-1}$. The fiber has a length $\ell = 10130 \pm 15 \text{ }\mu\text{m}$, width $w = 75 \pm 3 \text{ }\mu\text{m}$, height $h = 73 \pm 3 \text{ }\mu\text{m}$, Young's modulus $E = 27 \pm 7 \text{ kPa}$. The fluid viscosity is $\mu = 85 \pm 3 \text{ mPa}\cdot\text{s}$. Channel height and width are respectively $H = 85 \pm 3 \text{ }\mu\text{m}$ and $W = 3500 \text{ }\mu\text{m}$. Scale bar is $1000 \text{ }\mu\text{m}$. (b) Geometry of the fiber and the confining channel. The pressure-driven flow is sketched in blue.

ing during the transport of a flexible fiber in a viscous flow.

We first characterize the spatial and temporal evolution of the observed wave by studying the wavelength and the phase velocity of the perturbation as a function of the physical parameters of the system. Then, by the means of the linear Ginzburg-Landau model - the archetypal evolution model leading to an absolute or a convective instability [32] - we describe the spatio-temporal dynamics of the envelope and show the linear and local nature of the absolute instability as well as a near zero group velocity.

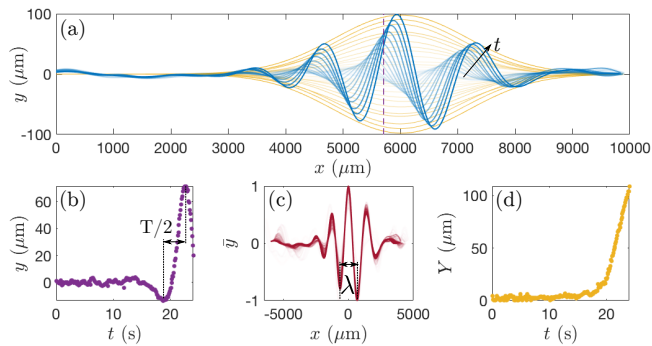


FIG. 2: Characterization of the fiber deformation. (a) Blue: Superposition of the shapes of the fiber shown in Fig. 1 in the reference frame of the fiber. Yellow: Superposition of the envelope of the deformation. Darker colors indicate later time points (time interval is 0.4 sec). (b) Temporal evolution of the deformation amplitude at a fixed x -location on the fiber (purple dashed line in (a)). The period of the oscillation, T , can be extracted from this curve. (c) Superposition of shapes normalized by their maximum ($\bar{y} = y/\max(y)$) and aligned on their maxima ($x = 0$). The wavelength of the deformation, λ , is constant. (d) Growth of the envelope amplitude with time.

Material and methods. Fibers are fabricated in a microchannel of Hele-Shaw geometry (see Figure 1 (b)), using the stop-flow microscope-based projection photolithography method [33, 34]. This method enables the fabrication, directly inside a microchannel, of polymeric PEG-based hydrogel particles of rectangular cross section, surrounded by a Newtonian solution of uncured PEGDA. It allows for an excellent control of the particle geometry and its mechanical properties [2, 35, 36]. Details can be found in references [2, 33, 35–40]. An important feature of this method is the existence of a liquid gap between the fiber and the channel top and bottom walls of constant height $b = 6.0 \pm 1.6 \mu\text{m}$. We use channels of fixed height $H = 85 \pm 3 \mu\text{m}$ and different widths ($W = 1000 \mu\text{m} - 3500 \mu\text{m}$). The resulting fiber height is $h = 73 \pm 3 \mu\text{m}$ leading to strong confinement by the top and bottom walls: $h/H = 0.86$. Fiber width varies from $w = 73 \mu\text{m}$ to $w = 118 \mu\text{m}$ while the length varies from $\ell = 9174 \pm 15 \mu\text{m}$ to $\ell = 15000 \pm 15 \mu\text{m}$ and Young modulus varies from $E = 117 \pm 64 \text{ kPa}$ to $E = 27 \pm 7 \text{ kPa}$.

Once a fiber is fabricated, flow is turned on with a syringe pump (Nemesys, Cetoni). Because of the Hele-Shaw geometry of the channel, the flow is plug-like in the (Oxy) plane, except in the vicinity of the lateral walls and of the fiber, and Poiseuille like in the (Oxz) plane (see Fig. 1 (b)). The fiber is imaged using an Hamamatsu Orca-flash 4.0 camera, at 10 fps. The fiber is kept in the camera's field of view by manually moving the microscope stage.

The fiber shapes are extracted from images by standard image processing (with ImageJ [41] and Matlab). The wavelength is measured by spatial Fourier transform while the envelope is obtained through an Hilbert transform.

Results The evolution of the shape of the fiber shown in Fig. 1 (a) is summarized in Fig. 2 (a). The fiber adopts a wavy shape (blue curves) whose amplitude decreases toward the edges as emphasized by the shape envelopes (plotted in yellow). Darker curves correspond to later time points and one can see that the deformation amplitude increases with time. In Fig. 2 (a) the back ends have been aligned to highlight that the wave propagates along the fiber from back to front at the phase velocity $V = \lambda/T$ with λ the wavelength and T the wave period. The wave period is measured by following the deformation amplitude y on a fixed abscissa as shown in Fig. 2 (b). The wavelength is shown to be constant by superposing normalized shapes aligned on their maxima (Fig. 2 (c)). As time increases, the deformation increases and spreads along the fiber (see Fig. 2 (a) and (d) and Figs. 4 (a) and (c) until saturation (not shown)). The evolution of the fiber velocity is given in Fig. 1 of the supp. data. After a transient regime the fiber velocity reaches a plateau value that precedes the mechanical instability.

To study the instability we first focus on the spatial and temporal evolution of the signal by characterizing the wavelength and the phase velocity of the wave. We characterize the dependence of the wavelength on the different parameters of the problem in Fig. 3. Contrary to classical buckling instabilities, the wavelength does not depend on the fiber length (Fig. 3 (a)) which indicates that the instability results from a local mechanism. However, perturbations are only observable for fibers one order of magnitude larger than λ (gray region at low ℓ in Fig. 3 (a)).

The deformation results from the competition between the elastic restoring force (F_{elast}) and a forcing by the hydrodynamic force (F_{visc}). By balancing these two forces one can build an elasto-viscous length Λ [8, 42, 43]:

$$F_{\text{elast}} = F_{\text{visc}} \Leftrightarrow EI/\Lambda^2 = \mu u_0 \Lambda \Leftrightarrow \Lambda = \left(\frac{F_{\text{elast}}}{F_{\text{visc}}} \right)^{1/3} \quad (1)$$

with u_0 the flow velocity, μ the fluid viscosity, E the

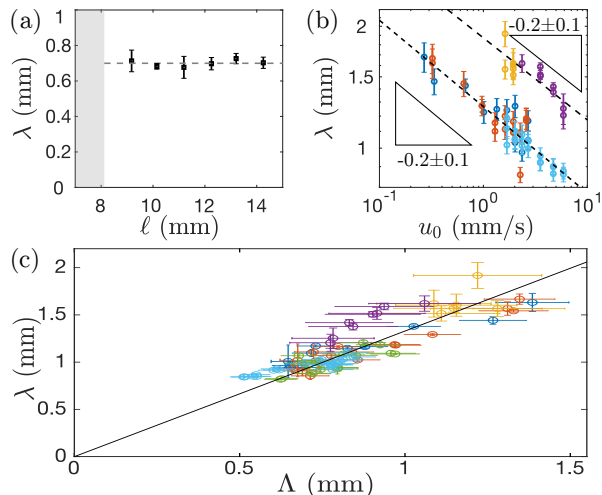


FIG. 3: Wavelength characterization. (a) Evolution of the wavelength λ as a function of the fiber length ℓ (all other parameters are kept constant. Fiber: $E = 0.20 \pm 0.11$ kPa, $w = 65 \pm 3 \mu\text{m}$, $h = 73 \pm 3 \mu\text{m}$. Channel: $W = 3500 \mu\text{m}$, $H = 85 \mu\text{m}$). (b) Evolution of λ as a function of u_0 . Two sets of data are represented gathering 59 experiments with different Young moduli, fiber lengths and channel widths, other parameter being constant ($w = 75 \pm 9 \mu\text{m}$, $h = 73 \pm 3 \mu\text{m}$, $H = 85 \pm 3 \mu\text{m}$). Yellow and purple: $E = 117 \pm 64$ kPa, $\ell = 15.64 \pm 0.47$ mm. Red, dark blue and light blue: $E = 27 \pm 7$ kPa, $\ell = 10.187 \pm 0.025$ mm. Red: $W = 3640 \pm 10 \mu\text{m}$; yellow and dark blue: $W = 3500 \pm 10 \mu\text{m}$; purple and light blue: $W = 1000 \pm 10 \mu\text{m}$. Dotted black lines correspond to fits by a power law. (c) Evolution of the wavelength as a function of the elasto-viscous length Λ . The data set is the same as in (b) (same color code) and has been complemented by the green points corresponding to variation of the width (from $73 \mu\text{m}$ to $118 \mu\text{m}$), other parameters being constant ($E = 27 \pm 7$ kPa, $\ell = 10.23 \pm 0.08$ mm, $h = 73 \pm 3 \mu\text{m}$ and $u_0 = 3.53$ mm/s). In total 72 measurements are shown in the figure. The dotted line corresponds to a linear fit of equation $\lambda = 1.33 \Lambda$.

Young modulus of the fiber and $I = \frac{hw^3}{12}$ its second moment of area.

To test this scaling we plotted in Fig. 3 (b) the evolution of the wavelength as a function of the flow velocity, for two different Young moduli, different channel widths and different fiber lengths. While the wavelength depends on flow velocity and Young modulus, it does not depend on channel width. Increasing u_0 or decreasing E results in a decrease of λ . The dependence of the wavelength on the flow velocity is nicely fitted by a power law $\lambda \propto u_0^\alpha$, with $\alpha = -0.2 \pm 0.1$ independent of E . These results are in fair agreement with the scaling given by equation (1) which predicts a decrease of the wavelength with the flow velocity as $\lambda \propto u_0^{1/3}$ and an increase with the Young modulus. Fig. 3 (c) gathers all the measurements shown in Fig. 3 (b) enriched with experiments where we varied the fiber width keeping the other parameters constant (green points). All wavelengths collapse onto a unique linear curve when plotted as a function

of the elasto-viscous length Λ , confirming Λ to be the relevant lengthscale of the system.

We also analyze the phase velocity V and show its proportionality to the mean flow velocity, with channel and fiber width having only a small impact (see Fig. 2 in the supp. data.).

To further describe the instability, including the envelop dynamics, we plot the spatio-temporal evolution of the fiber shape (see Fig. 4 (a)). Here, x -axis is the position along the fiber and the color code gives the deformation of the fiber in the perpendicular direction while time is represented on the vertical axis from bottom to top. The perturbation is initiated at roughly the center of the fiber - region where potential ends effect are less likely to occur - and grows and spreads as time increases. The signal can be described as a traveling wave modulated by an amplitude (see Fig. 4 (b)):

$$y(x, t) = \text{Re} \left\{ Y(x, t) e^{i \frac{2\pi}{\lambda} (x - Vt)} \right\}, \quad (2)$$

with $Y(x, t)$ the amplitude of the envelope, a function of time and position.

On Figs. 4 (a) and (b) we observe that the perturbation eventually invades all the fiber which indicates of an *absolute instability*. Consequently we use the linear and real Ginzburg-Landau (G-L) amplitude equation [44] to describe the instability:

$$\frac{\partial Y}{\partial t} = \sigma_0 Y - U \frac{\partial Y}{\partial x} + A \frac{\partial^2 Y}{\partial x^2}, \quad (3)$$

where σ_0 , U and A , are the growth rate, the group velocity, and the diffusion coefficient of the envelope.

The general solution of equation (3), for a Dirac perturbation of amplitude Y_0 at time t_0 and position x_0 , is a Gaussian function [45]:

$$Y(x, t) = \Phi(t) e^{-\frac{(x - X(t))^2}{\Delta(t)}}, \quad (4)$$

with the three quantities:

$$\Delta(t) = 4A(t - t_0), \quad (5)$$

$$\Phi(t) = -Y_0 / \left(2\pi \sqrt{2A(t - t_0)} \right) e^{\sigma_0(t - t_0)} \quad (6)$$

$$\text{and } X(t) = x_0 + U(t - t_0) \quad (7)$$

that only depend on time.

We then fit the envelope extracted from the experiments by a Gaussian function for every instant (see Fig. 4 (b)) to obtain Δ , Φ and X as a function of time (see Fig. 4 (d), (e) and (f)). The temporal evolutions of these parameters are in good agreement with the equations (5-7) as shown by the dotted curves in Fig. 4 (d-f) that result from the fitting of the data. The values of A , t_0 , σ_0 , U and x_0 extracted from the fitting procedure are then used to build the solution of the Ginzburg-Landau equation $Y(x, t)$. Fig. 4 (c) shows the resulting

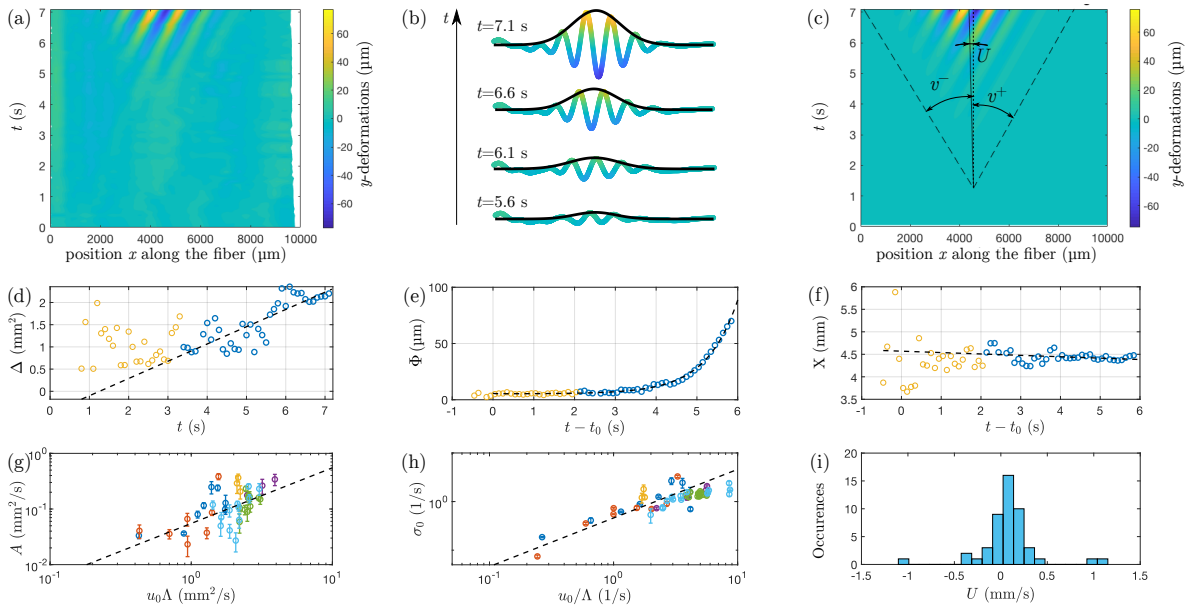


FIG. 4: (a) Fiber shape as a function of time. Experimental conditions are: $u_0 = 3.53$ mm/s, $E = 27 \pm 7$ kPa, $w = 83 \pm 3$ μm , $h = 73 \pm 3$ μm and $\mu = 85 \pm 3$ mPa.s. (b) A few (x, y) shape extracted from (a) illustrating the colour-code used in (a). Black curves are Gaussian fits of the envelope. (c) Same representation as (a) for a Ginzburg-Landau solution using parameters adjusted from the experiment shown in (a) and (b) (see text for details) $A = 9.7 \pm 1.9 \times 10^4$ $\mu\text{m}^2/\text{s}$, $t_0 = 1.3 \pm 0.8$ s, $x_0 = 4.57 \pm 0.12$ mm, $U = -31 \pm 29$ $\mu\text{m}/\text{s}$, $\sigma_0 = 1.37 \pm 0.07$ s^{-1} . v^+ and v^- are the velocity of the leading and trailing edges of the wave ($v^\pm = U \pm \sqrt{4A\sigma_0}$). (d), (e) and (f) correspond respectively to the evolution of Δ , Φ and X as a function of time. Dotted black curves represent fits with the equations (5-7). Only blue dots are taken into account for the fits, yellow dots are excluded because they derive from measurements of small deformations and are poorly reliable. (g) Diffusion coefficient of the envelope A as a function of $u_0\Lambda$ and (h) growth rate σ_0 as a function of u_0/Λ fitted from the different experiments shown in Fig.3 (same color code). The dotted black lines are of slope unity. (i) Histogram of the group velocity U . The set of experiments is the same as in Fig. 3.

spatio-temporal evolution which is in excellent agreement with the experimental observations (Fig. 4 (a)) confirming that this new instability is indeed *local and linear*.

To link the ad-hoc description of the system dynamics with the linear G-L equation to the physics of the underlying problem we determine the evolution of A , σ_0 and U as a function of u_0 , w and E . We observe that the diffusion coefficient A scales reasonably well as $u_0\Lambda$ (see Fig. 4 (g)). Fig. 4 (h) shows the evolution of the growth rate σ_0 as a function of u_0/Λ . All points collapse fairly well onto a master curve, confirming that the characteristic length of the system is Λ and that all velocities are proportional to u_0 . Lastly, as visible in Fig. 4 (i), U is always close or equal to zero, i.e. the center of the envelope only slightly moves along the fibers.

Conclusion When sufficiently long i.e. $\ell \gg \Lambda$, a parallel fiber transported by an external flow in a confining geometry - the fiber height being similar to the channel height - experiences an instability. The fiber deforms in a wavy shape modulated by an envelope which spreads along the fiber and whose amplitude increases with time. We show that the wavelength is constant with time and does not depend on the fiber length. It is set instead by the elasto-viscous length Λ on which elastic forces bal-

ance hydrodynamic forces. By investigating the spatio-temporal evolution of the signal we confirm that we witness an *absolute* instability arising from a *local* amplification mechanism. We show that the dynamics of the amplitude and the spreading of the envelope are well described by the linear Ginzburg-Landau equation and the overall envelope dynamics is completely captured by three parameters: a group velocity U , a diffusion coefficient A and a growth rate σ_0 . In all our experiments the group velocity is close to zero, meaning that the envelope only slightly moves along the fibers. On the contrary, the wavelength, the phase velocity, the growth rate and the diffusion coefficient all depend on Λ and/or on u_0 . All velocities are proportional to the flow velocity as expected in viscous flows. As Λ takes into account all the physical ingredients of the system we can claim that the instability is fully described by a competition between two forces: a destabilising hydrodynamic force and a restoring elastic force. In light of these conclusions we attempted several approaches to derive a dispersion relation (see reference [46]), however further efforts are necessary for a full understanding of the detailed mechanisms.

-
- [1] O. du Roure, A. Lindner, E. Nazockdast, and M. Shelley, *Annual Review of Fluid Mechanics* (2019).
- [2] J. Cappello, M. Bechert, C. Duprat, O. du Roure, F. Gallaire, and A. Lindner, *Physical Review Fluids* **4**, 034202 (2019).
- [3] B. Marchetti, V. Raspa, A. Lindner, O. du Roure, L. Bergougnoux, É. Guazzelli, and C. Duprat, to be submitted pp. 1–23 (2018).
- [4] L. Li, H. Manikantan, D. Saintillan, and S. E. Spagnolie, *Journal of Fluid Mechanics* **735**, 705 (2013), ISSN 0022-1120, 1306.4692, URL [http://www.journals.cambridge.org/abstract_{_}S0022112013005120](http://www.journals.cambridge.org/abstract/S0022112013005120).
- [5] L. Guglielmini, A. Kushwaha, E. S. Shaqfeh, and H. A. Stone, *Physics of Fluids* **24**, 123601 (2012).
- [6] Y.-N. Young and M. J. Shelley, *Physical review letters* **99**, 058303 (2007).
- [7] E. Wandersman, N. Quennouz, M. Fermigier, A. Lindner, and O. Du Roure, *Soft matter* **6**, 5715 (2010).
- [8] B. Chakrabarti, Y. Liu, J. LaGrone, R. Cortez, L. Fauci, O. du Roure, D. Saintillan, and A. Lindner, *Nature Physics* **16**, 689 (2020).
- [9] Y. Liu, B. Chakrabarti, D. Saintillan, A. Lindner, and O. Du Roure, *Proceedings of the National Academy of Sciences* **115**, 9438 (2018).
- [10] O. Forgacs and S. Mason, *Journal of Colloid Science* **14**, 473 (1959).
- [11] M. Harasim, B. Wunderlich, O. Peleg, M. Kröger, and A. R. Bausch, *Physical review letters* **110**, 108302 (2013).
- [12] H. Nguyen and L. Fauci, *Journal of The Royal Society Interface* **11**, 20140314 (2014).
- [13] L. E. Becker and M. J. Shelley, *Physical Review Letters* **87**, 198301 (2001).
- [14] N. Quennouz, M. Shelley, O. Du Roure, and A. Lindner, *J Fluid Mech* **769**, 387 (2015).
- [15] H. Manikantan and D. Saintillan, *Physics of Fluids* **25**, 073603 (2013).
- [16] D. Steinhäuser, S. Köster, and T. Pfohl, *ACS Macro Letters* **1**, 541 (2012).
- [17] H. Manikantan and D. Saintillan, *Physical Review E* **92**, 041002 (2015).
- [18] Y. Liu, K. Zografos, J. Fidalgo, C. Duchêne, C. Quintard, T. Darnige, F. Vasco, S. Huille, O. du Roure, M. S. Oliveira, et al., *Soft Matter* (2020).
- [19] X. Xu and A. Nadim, *Physics of Fluids* **6**, 2889 (1994), ISSN 1070-6631, URL <http://scitation.aip.org/content/aip/journal/pof2/6/9/10.1063/1.868116>.
- [20] M. V. D'Angelo, B. Semin, G. Picard, M. E. Poitzsch, J. P. Hulin, and H. Auradou, *Trans. Porous Med.* **84**, 389 (2009), ISSN 0169-3913, URL <http://link.springer.com/10.1007/s11242-009-9507-x>.
- [21] M. D'Angelo, H. Auradou, G. Picard, M. Poitzsch, and J. Hulin, in *Journal of Physics: Conference Series* (IOP Publishing, 2009), vol. 166, p. 012001.
- [22] G. S. Triantafyllou, K. Kupfer, and A. Bers, *Physical review letters* **59**, 1914 (1987).
- [23] P. Gondret, P. Ern, L. Meignin, and M. Rabaud, *Physical review letters* **82**, 1442 (1999).
- [24] F. Charru, *Instabilités hydrodynamiques* (EDP Sciences, 2012).
- [25] P. Huerre, G. Batchelor, H. Moffatt, and M. Worster, *Perspectives in fluid dynamics* pp. 159–229 (2000).
- [26] A. S. Utada, A. Fernandez-Nieves, J. M. Gordillo, and D. A. Weitz, *Physical review letters* **100**, 014502 (2008).
- [27] J. M. Gordillo, A. M. Gañán-Calvo, and M. Pérez-Saborid, *Physics of fluids* **13**, 3839 (2001).
- [28] A. M. Gañán-Calvo et al., *Journal of Fluid Mechanics* **553**, 75 (2006).
- [29] P. Guillot, A. Colin, A. S. Utada, and A. Ajdari, *Physical review letters* **99**, 104502 (2007).
- [30] C. Duprat, C. Ruyer-Quil, S. Kalliadasis, and F. Giorgiutti-Dauphiné, *Physical review letters* **98**, 244502 (2007).
- [31] F. Gallaire and P.-T. Brun, *Philosophical Transactions of the Royal Society A: Mathematical, Physical and Engineering Sciences* **375**, 20160155 (2017).
- [32] P. Huerre and P. A. Monkewitz, *Annual review of fluid mechanics* **22**, 473 (1990).
- [33] D. Dendukuri, P. Panda, R. Haghgoie, J. M. Kim, T. A. Hatton, and P. S. Doyle, *Macromolecules* **41**, 8547 (2008), ISSN 00249297.
- [34] D. Dendukuri, S. S. Gu, D. C. Pregibon, T. A. Hatton, and P. S. Doyle, *Lab on a Chip* **7**, 818 (2007), ISSN 1473-0197, URL <http://xlink.rsc.org/?DOI=b703457a>.
- [35] C. Duprat, H. Berthet, J. S. Wexler, O. du Roure, and A. Lindner, *Lab on a chip* **15**, 244 (2014), ISSN 1473-0189, URL <http://www.ncbi.nlm.nih.gov/pubmed/25360871>.
- [36] J. Cappello, V. D'herbemont, A. Lindner, and O. Du Roure, *Micromachines* **11**, 318 (2020).
- [37] J. S. Wexler, P. H. Trinh, H. Berthet, N. Quennouz, O. du Roure, H. E. Huppert, A. Linder, and H. A. Stone, *Journal of Fluid Mechanics* **720**, 517 (2013), ISSN 0022-1120, URL [http://www.journals.cambridge.org/abstract_{_}S0022112013000499](http://www.journals.cambridge.org/abstract/S0022112013000499).
- [38] H. Berthet, O. du Roure, and A. Lindner, *Applied Sciences* **6**, 385 (2016), ISSN 2076-3417, URL <http://www.mdpi.com/2076-3417/6/12/385>.
- [39] M. Nagel, P.-T. Brun, H. Berthet, A. Lindner, F. Gallaire, and C. Duprat, *Journal of Fluid Mechanics* **835**, 444 (2018).
- [40] M. Bechert, J. Cappello, M. Daëff, F. Gallaire, A. Lindner, and C. Duprat, *EPL (Europhysics Letters)* **126**, 44001 (2019).
- [41] C. A. Schneider, W. S. Rasband, and K. W. Eliceiri, *Nature Methods* **9**, 671 (2012), ISSN 1548-7091, URL <http://dx.doi.org/10.1038/nmeth.2089>.
- [42] F. Gosselin, P. Neetzow, and M. Paak, *Physical Review E* **90**, 052718 (2014).
- [43] N. Coq, O. Du Roure, J. Marthelot, D. Bartolo, and M. Fermigier, *Physics of Fluids* **20**, 051703 (2008).
- [44] C. Godreche and P. Manneville, *Oceanographic Literature Review* **9**, 1723 (1998).
- [45] B. Castaing, *Hydrodynamics and nonlinear instabilities*, vol. 3 (Cambridge University Press, 2005).
- [46] J. Cappello, Phd thesis, Université de Paris (2020), URL <https://tel.archives-ouvertes.fr/tel-03260710>.